Harmonic Compensation Strategy for Single-Phase Cascaded H-Bridge PV Inverter under Unbalanced Power Conditions

Mingda Wang, Xing Zhang, *Senior Member, IEEE*, Tao Zhao, *Student Member, IEEE*, Mingyao Ma, *Member, IEEE*, Yuhua Hu, Fusheng Wang, *Member, IEEE*, and Xinyu Wang

***Abstract*—Cascaded H-bridge (CHB) inverter has the advantages of easy modularization, the low harmonic content of output current, and that all power units are capable of achieving independent MPPT. However, aging or partial shielding of photovoltaic (PV) panels will lead to the unbalanced output power of each PV module, which will result in the overmodulation of H-bridges (HBs) and increased harmonic components of the grid current. In this paper, a novel harmonic compensation strategy for single-phase CHB inverter is proposed, it can extend the linear modulation range of single-phase CHB inverters to about 1.27. Moreover, this strategy will not reduce energy harvesting, and also can maintain the system to operate in the unit power factor. Simulation and experimental results all verify the effectiveness of the proposed strategy.**

***Index Terms*—single-phase inverter, cascaded H-bridge, overmodulation, power imbalance.**

I. Introduction

As the problems of energy shortage and environmental pollution have been the focus of the world, developing a low-carbon economy and transforming the traditional pattern of energy-intensive economic growth are becoming common choices for all countries [1]. Due to easy access and conversion, solar energy has become the fastest growing renewable energy source [2].

Multilevel inverters have been attracting worldwide attention due to their low switching stress, low filter inductance, and high system efficiency [3],[4]. There are many topologies of the multilevel inverter, including diode clamped, flying capacitor, and cascaded H-bridge [5],[6]. With the same number of output levels, CHB has the smallest number of devices [7]. In addition, the dc side of each power unit in CHB is powered by a PV module independently so that it can implement independent MPPT. Therefore, CHB inverter is an ideal choice for PV grid-connected power generation system [8]-[9].

One of the key issues of CHB inverters is the power imbalance among HBs. Due to aging, damage or partial shielding of PV panels, the output powers of some HBs decrease severely, which makes the HBs with higher power over-modulation and leads to a distorted grid current [10]-[11]. To deal with this issue, several control strategies have been proposed. In [12], a modified MPPT (MMPPT) algorithm is proposed, which makes PV modules with higher output power quit MPPT operation to balance the output powers, but this will reduce energy harvesting of the whole system. A hybrid modulation strategy (HMS) is presented in [13]-[17]. This strategy combines low-frequency square waveform with high-frequency PWM waveform to expand the linear modulation range of the inverter. It can suppress harmonics of grid current very well and extend the linear modulation range to about $4/\pi$. However, HMS sorts the differences between dc-link measured voltages and corresponding reference voltages in ascending order, then makes HBs with higher difference discharged and those with lower difference charged according to the operating state of system. Compared with SPWM using PI controllers to precisely regulate dc-link voltage, HMS will aggravate the voltage fluctuation on the dc side, and this will reduce the efficiency of MPPT [15],[16]. In [18]-[20], a reactive power compensation strategy (RPCS) is proposed, it can reduce the THD of grid current without aggravating the fluctuation of dc-link voltage, but it will lower the system power factor (PF), which limits the application of RPCS.

A third harmonic compensation strategy (THCS) for three-phase CHB inverters is proposed in [21]-[23]. Both of them use a harmonic injection method to solve the problem of inter-phase power imbalance in three-phase CHB inverters. Then, a third harmonic compensation strategy for single-phase CHB inverters is presented in [24],[25], which solves the shortcomings of the above methods effectively. That is, it does not reduce the power generation, and ensures that the system can operate with unit power factor and the fluctuation of dc-link voltage is also relatively small. However, the maximum linear modulation range of THCS is only extended to 1.155, so the ability to deal with power imbalance is relatively weaker.

Based on this point, a novel harmonic compensation strategy (HCS) is proposed in this paper. By injecting multiple harmonics to the overmodulation HBs, this strategy can transform the overmodulation waveform into the quasi-square

Manuscript received May 30, 2019; revised July 19, 2019, and October 27, 2019; accepted December 14, 2019. (*Corresponding author: Mingyao Ma.*) This work was supported by the National Key R&D Program of China (2018YFB1500703).

Mingda Wang, Xing Zhang, Tao Zhao, Mingyao Ma, Yuhua Hu and Fusheng Wang are with the National and Local Joint Engineering Laboratory for Renewable Energy Access to Grid Technology, Hefei University of Technology, Hefei 230009, China (e-mail: wmd6094@mail.hfut.edu.cn; honglf@ustc.edu.cn; zt_kyyx@163.com; miyama@hfut.edu.cn; hfut_HYH@163.com; 10748451@qq.com;).

Xinyu Wang is with Sungrow Power Supply Co., Ltd., Hefei 230088, China (e-mail: wxyrock@126.com).

waveform. At the same time, in order to ensure that the output voltage of the inverter does not contain the injected harmonic components, the equivalent but inverse harmonics are injected to the non-overmodulation HBs. HCS takes advantages of the characteristic that the fundamental amplitude of the square wave is 4/π, and extends the linear modulation range to about 1.27. Since HCS and THCS are both harmonic compensation methods, HCS can also preserve the advantages of THCS. Both simulation and experimental results verify the effectiveness of this proposed strategy.

This paper is organized as follows: the system configuration and stability domain are analyzed in Section II. Harmonic compensation method and system control strategy are covered in Section III. Simulation results are demonstrated in Section IV, and experimental results are presented in Sections V. The last part is the conclusions in Section VI.

II. System Configuration And Analysis

The schematic diagram of a single-phase CHB PV inverter is presented in Fig.1. It consists of *n* HBs, and the dc side of each HB is independently powered by a PV module. The ac side is connected to the power grid through an inductor. Each HB is able to output three levels of 1, 0, and -1, so its output voltage can reach 2*n*+1 levels. v_{grid} and i_{grid} are grid voltage and current, respectively; V_{dci} and I_{pvi} are the dc-link voltage and current of the *i*th (*i*=1,2,3...*n*) HB, respectively; v_{Hi} is the output voltage of the *i*th HB module. L and C_i represent filter inductor and *i*th module dc-bus capacitor, respectively.

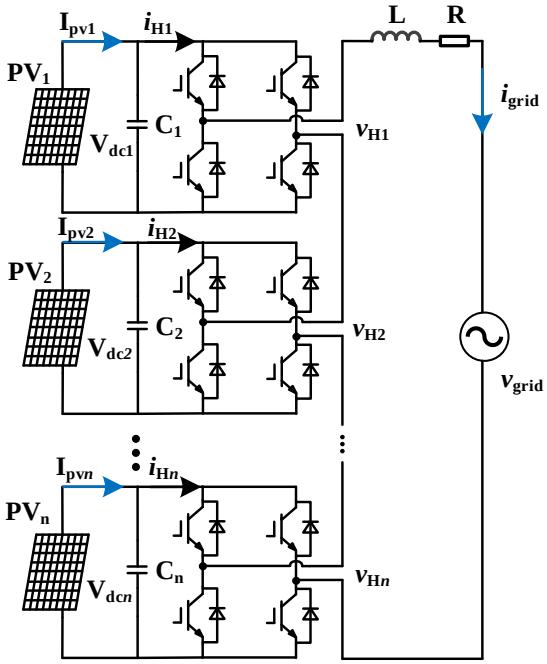

Fig.1 Schematic diagram of single-phase CHB PV grid-connected inverter.

Due to damage or occlusion, the output powers of some PV panels may decrease dramatically, and the rest still maintain the original output powers, resulting in a decrease in the total output power (P_T) of CHB inverter. Since the RMS value of grid voltage, V_{grid}, remains unchanged, the RMS value of grid current, I_{grid}, will decrease. For the CHB inverter, all HBs carry the same current (that is i_{grid}), so the output voltage of the unshaded cells (whose output power does not decrease) will rise, which will lead to an increased modulation waveform amplitude and increases the risk of overmodulation.

For the CHB inverter, the modulation waveform (k_i) of the *i*th HB can be expressed as:

$$k_i = \frac{v_{HFi}}{V_{dci}} \tag{1}$$

where v_{HFi} is the fundamental component of v_{Hi}.

According to the topology in the Fig.1, the dynamic characteristics of the CHB system can be expressed as:

$$i_{Hi} = k_i i_{grid} \tag{2}$$

$$\frac{dV_{dci}}{dt} = \frac{1}{C_i}\left(I_{pvi} - i_{Hi}\right) \tag{3}$$

$$\frac{di_{grid}}{dt} = \frac{1}{L}\left(\sum_{i=1}^{n} k_i V_{dci} - R i_{grid} - v_{grid}\right) \tag{4}$$

In order to facilitate analysis, the phase theory is used to analyze the stability region of the CHB inverter and ac variables are expressed in RMS. Ignoring the equivalent resistance R, the expression (4) can be rewritten as:

$$\sum_{i=1}^{n} \boldsymbol{K}_i V_{dci} = \sum_{i=1}^{n} \boldsymbol{V}_{HFi} = \boldsymbol{V}_{grid} + j\omega L \boldsymbol{I}_{grid} \tag{5}$$

where ω is the angular frequency of the grid, $\boldsymbol{K_i}$ is the phasor form of k_i and $\boldsymbol{V_{HFi}}$ is the phasor form of v_{HFi}, $\boldsymbol{V_{grid}}$ and $\boldsymbol{I_{grid}}$ are the phasor forms of v_{grid} and i_{grid}, respectively.

As shown in Fig.2, when the inverter is operated in the unit power factor state, the phasor diagram can be acquired from (5), where the voltage component of inductance L is very small compared with the grid voltage so that the angle δ can be approximated as zero.

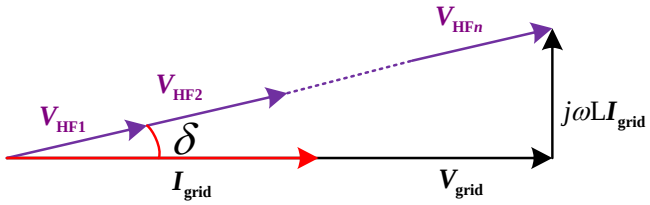

Fig.2. Phasor diagram of CHB PV grid-connected inverter.

The active power output (P_i) of the *i*th HB can be obtained as follows:

$$P_i = \left|\boldsymbol{V}_{HFi}\right|\left|\boldsymbol{I}_{grid}\right|\cos\delta \approx \left|\boldsymbol{K}_i\right|\left|\boldsymbol{I}_{grid}\right| V_{dci} = K_i V_{dci} I_{grid} \tag{6}$$

where K_i is the RMS of k_i.

The power losses of equivalent resistances and switching devices can be ignored, so:

$$P_i = K_i V_{dci} I_{grid} = V_{dci} I_{pvi} \tag{7}$$

From (7), because K_i is the RMS value of k_i, the condition of not be overmodulation when using SPWM is shown as follows:

$$\sqrt{2} K_i \le 1 \tag{8}$$

Based on (7) and (8), the condition of non-overmodulation is as follows:

$$I_{grid} \geq \sqrt{2} I_{pvi} \tag{9}$$

Therefore, if only one HB in the system does not satisfy (9), i_{grid} will be distorted due to overmodulation.

III. Modulation Method and Control Strategy

From the above analysis, when the output powers of some HBs decrease seriously, the cells (HBs) with higher output power may suffer from overmodulation. Therefore, it is necessary to adopt some methods to deal with this issue. On the basis of the methods in [24],[25], a HCS, which extends the maximum linear modulation range of HBs to about 1.27, is proposed to make the system operate normally under severely unbalanced power conditions.

A. Harmonic compensation strategy

For the cosine modulation waveform with the amplitude $\hat{M}$ greater than one, shown in Fig.3, its expression is as follows:

$$f(x) = \hat{M}\cos x \tag{10}$$

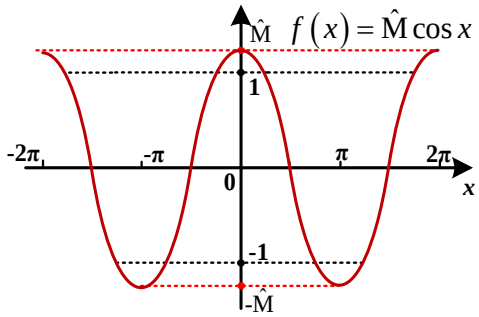

Fig.3. Waveform of $f(x)$.

Define a compensation harmonic hf, which is superimposed on $f(x)$ to change it to a quasi-square waveform. The modulation waveform after compensation is acquired:

$$g(x) = f(x) + hf = \hat{M}\cos x + hf \tag{11}$$

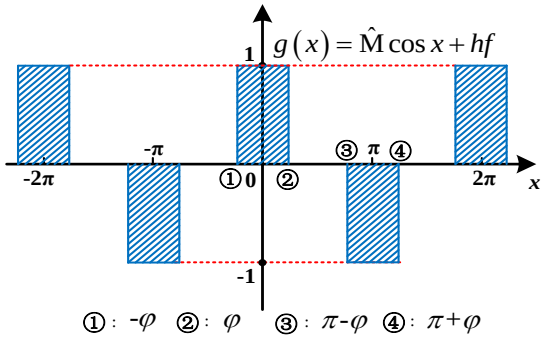

Fig.4. Waveform of $g(x)$.

Fig.4 shows the waveform of $g(x)$, and its expression is (12).

$$g(x) = \begin{cases} 0 & -\pi+\varphi+2k\pi \leq x < -\varphi+2k\pi \\ 1 & -\varphi+2k\pi \leq x < \varphi+2k\pi \\ 0 & \varphi+2k\pi \leq x < \pi-\varphi+2k\pi \\ -1 & \pi-\varphi+2k\pi \leq x < \pi+\varphi+2k\pi \end{cases} \tag{12}$$
$$(k = 0, \pm 1, \pm 2\ldots)$$

where φ is the conduction angle of $g(x)$.

Take the Fourier decomposition of $g(x)$, and the Fourier series is:

$$g(x) = \frac{a_0}{2} + \sum_{n=1}^{\infty}\left(a_n \cos(nx) + b_n \sin(nx)\right) \tag{13}$$

Since $g(x)$ is an even function, its Fourier series can be simplified accordingly:

$$a_0 = b_1 = 0 \tag{14}$$

$$a_1 = \frac{1}{\pi}\int_{-\pi}^{\pi} g(x)\cos x dx = \frac{4}{\pi}\sin\varphi \tag{15}$$

From (13), (14), (15), the $g(x)$ fundamental component $B(x)$ can be acquired:

$$B(x) = a_1 \cos x = \hat{B}\cos x \tag{16}$$

$$\hat{B} = \frac{4}{\pi}\sin\varphi \tag{17}$$

That is to say, for a cosine modulation waveform whose amplitude is $\hat{M}$, it can be changed to a quasi-square waveform with fundamental waveform amplitude is $\hat{B}$ through injecting harmonic hf.

Based on (10), (16) and (17), making the $\hat{B}$ is equal to $\hat{M}$, the conduction angle φ of $g(x)$ can be calculated as:

$$\varphi = \arcsin\left(\frac{\pi}{4}\hat{M}\right) \tag{18}$$

Therefore, if the conduction angle φ satisfies (18), the fundamental component of $g(x)$ is the same as $f(x)$.

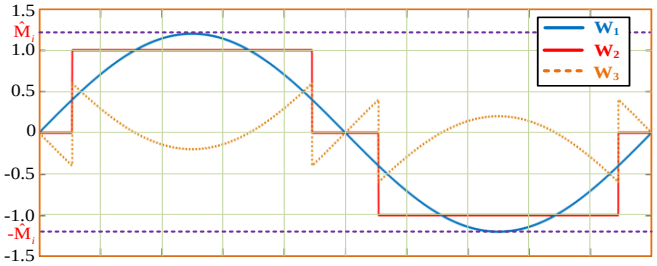

Fig.5. Schematic diagram of the proposed strategy.

Fig.5 illustrates the principle of the proposed HCS. For a CHB inverter, if the ith HB is overmodulated, and its modulation waveform is the curve W_1 in Fig.5 ($\hat{M}_i$ >1). To change the amplitude of W_1 not larger than one, the curve W_2 can be acquired from (12) and (18). And the curve W_3 is the injected harmonic which can be calculated by W_2-W_1. From the above analysis, the fundamental component of W_2 is the same with W_1. W_2 is a quasi-square waveform with the amplitude of one, and there is no longer the problem of overmodulation.

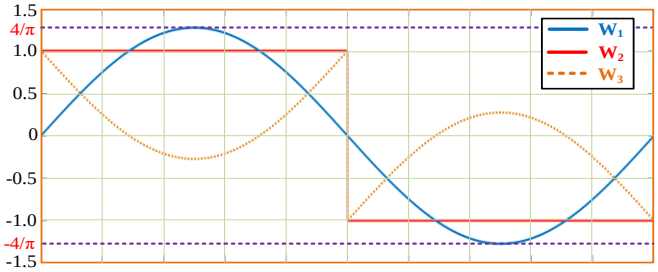

Fig.6. Schematic diagram of the proposed strategy when $\hat{M}_i$ is 4/π.

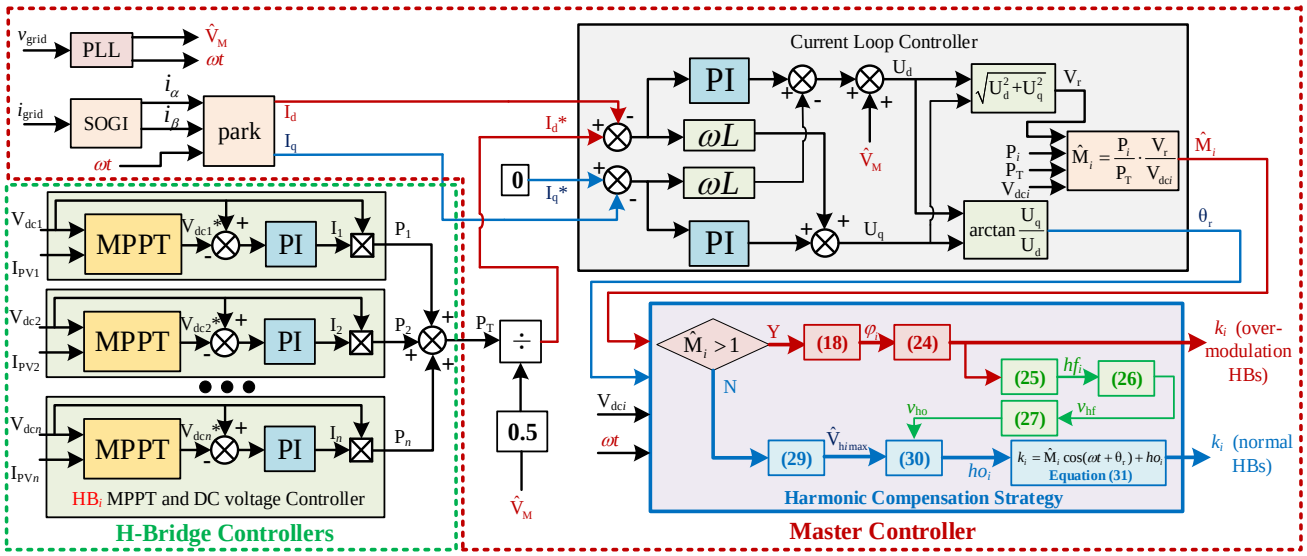

Fig.7 Block diagram of system control strategy.

According to (16) and (17), the max fundamental component amplitude ($\hat{B}_{max}$) of $g(x)$ can be acquired:

$$\hat{B}_{max} = \frac{4}{\pi} \approx 1.27 \tag{19}$$

That is, the maximum amplitude of the overmodulation waveform that the proposed HCS can deal with is 4/π (about 1.27). Fig.6 shows the corresponding waveforms of the proposed HCS when the amplitude of the overmodulation waveform is 4/π. It can be seen that there is no room for the square wave to continue to expand.

B. System control strategy

In this paper, the control block diagram of single-phase CHB inverter is shown in Fig.7. The single-phase CHB inverter is composed of *n* HBs, each HB has a controller for independent control, which is mainly responsible for MPPT, dc voltage control of each HB and transmitting the output powers to the master controller.

The master controller receives the output powers of all HBs and adds them together to obtain the total power P_T.

$$P_T = \frac{1}{2}\hat{V}_M \hat{I}_M \tag{20}$$

where, $\hat{V}_M$ and $\hat{I}_M$ are the amplitude of v_{grid} and i_{grid}, respectively. The active power reference current (I_d^*) is acquired by dividing P_T by the half of $\hat{V}_M$, in which $\hat{V}_M$ and phase information (ωt) of v_{grid} are provided by a phase-locked loop (PLL). Because of the single-phase inverter, i_{grid} lacks one degree of freedom to achieve the coordinate rotation transformation of the ac quantity. Therefore, two orthogonal signals i_α and i_β need to be obtained by second-order generalized integral transformation (SOGI), where i_α has the same frequency and phase as i_{grid} and i_β lags behind i_α 90 degrees. Since the two orthogonal signals i_α, i_β and phase information ωt are acquired, the current loop control feedback signal I_d and I_q are got through Park transformation. Generally, the reactive power reference current (I_q^*) is set as zero.

By PI controllers and relevant calculation, the current loop outputs the amplitude (V_r) of the total modulation voltage, and the angle (θ_r) between the total modulation voltage and the grid voltage. After obtaining the total modulation voltage, the modulation voltage of each HB needs to be further allocated. since output currents of all HB are the same, the power ratio of each HB is the ratio of their ac-side output voltages:

$$\frac{\hat{V}_1}{P_1} = \frac{\hat{V}_2}{P_2} = \bullet\bullet\bullet = \frac{\hat{V}_n}{P_n} = \frac{\hat{V}_r}{P_T} \tag{21}$$

where, $\hat{V}_i$ denote the amplitudes of v_{Hi}. From (1) and (21), the modulation waveform amplitude ($\hat{M}_i$) of each HB can be obtained as follows:

$$\hat{M}_i = \frac{\hat{V}_i}{V_{dci}} = \frac{\hat{V}_i}{V_r}\frac{V_r}{V_{dci}} = \frac{P_i}{P_T}\frac{V_r}{V_{dci}} \tag{22}$$

After obtaining the $\hat{M}_i$ of each HB, it can be determined which HB is overmodulation. If all HBs are not overmodulated, the modulation waveforms of each HB are calculated by the following formula:

$$k_i = \hat{M}_i \cos(\omega t + \theta_r) \tag{23}$$

As long as an overmodulation module exists, the HCS proposed in this paper will be used to output the modulation waveform of each HB.

According to the HCS flowchart shown in Fig.7, assuming that the first to the *m*th HBs are the overmodulated cells (the $\hat{M}_i$ is not more than 1.27), and the other HBs are not overmodulated ($1 < \hat{M}_1 \sim \hat{M}_m < 1.27$ and $0 < \hat{M}_{m+1} \sim \hat{M}_n < 1$). For the overmodulation HBs, the angle φ_i (i=1,2…m) can be calculated according to (18) and (22), then the modulation waveforms k_i (i=1,2…m) can be calculated as follows:

$$k_i = g_i(x) = \begin{cases} 0 & -\pi + \varphi_i + 2k\pi \le x < -\varphi_i + 2k\pi \\ 1 & -\varphi_i + 2k\pi \le x < \varphi_i + 2k\pi \\ 0 & \varphi_i + 2k\pi \le x < \pi - \varphi_i + 2k\pi \\ -1 & \pi - \varphi_i + 2k\pi \le x < \pi + \varphi_i + 2k\pi \end{cases} \tag{24}$$

From the analysis above, the fundamental waveform amplitudes of k_i are equal to $\hat{M}_i$. Therefore, the harmonics hf_i (i=1,2…m) compensated to the overmodulation HBs are:

$$hf_i = k_i - \hat{M}_i \cos(\omega t + \theta_r) \quad i = 1, 2...m \tag{25}$$

Thus, the total compensation harmonic voltage (v_{hf}) of the overmodulation HBs is obtained as follows:

$$v_{hf} = \sum_{i=1}^{m} (hf_i \cdot V_{dci}) = \sum_{i=1}^{m} [k_i - \hat{M}_i \cos(\omega t + \theta_r)] V_{dci} \tag{26}$$

In order to make the total output voltage of CHB system not contain the injected harmonics, the modulation waveform of the normal HBs need to compensate harmonics ho_i (i=m+1, …, n), whose phase is opposite to hf_i.

Therefore, the harmonic voltage (v_{ho}) injected into the normal HBs is:

$$v_{ho} = -v_{hf} = \sum_{i=1}^{m} (\hat{M}_i \cos(\omega t + \theta_r) - k_i) V_{dci} \tag{27}$$

It is worth noting that the amplitude of actual modulation waveform of an overmodulation HB will decrease after compensating hf_i (because it has become a quasi-square waveform with the amplitude is one), but that of a normal HB will increase after compensating ho_i. In order to ensure that the normal HBs do not overmodulate due to compensating ho_i, it is necessary to calculate the maximum compensation harmonic voltage $v_{hi\max}$ (i=m+1, …, n) allowed by each normal cell.

$$v_{hi\max} = [(1 - \hat{M}_i)\cos(\omega t + \theta_r)] V_{dci} \quad i = m+1, ..., n \tag{28}$$

Furthermore, the maximum compensation voltage amplitude $\hat{V}_{hi\max}$ (i=m+1, …, n) of the normal HBs is obtained:

$$\hat{V}_{hi\max} = (1 - \hat{M}_i) V_{dci} \quad i = m+1, ...n \tag{29}$$

Therefore, the normal HBs can distribute v_{ho} according to the maximum harmonic compensation voltage amplitude of each normal HB can bear, and the compensation harmonic ho_i (i=m+1, …, n) of each normal HB is as follows:

$$ho_i = \frac{v_{ho}}{V_{dci}} \cdot \frac{\hat{V}_{hi\max}}{\sum_{m+1}^{n} \hat{V}_{hi\max}} \quad i = m+1, ..., n \tag{30}$$

Finally, the modulation waveforms of the normal HBs are obtained as follows:

$$k_i = \hat{M}_i \cos(\omega t + \theta_r) + ho_i \quad i = m+1, ..., n \tag{31}$$

It should be noted that in the absence of HB over-modulation (0< $\hat{M}_1$ ~ $\hat{M}_n$ <1), all HB modulation waveforms will be calculated by (31) according to the flowchart of HCS in Fig.7. But the ho_i is zero in this case, so the modulation waveforms will eventually be generated by (23).

IV. Simulation Results

To verify the effectiveness of the proposed strategy, a single-phase CHB model with five HBs was built in MATLAB/Simulink. The PV module parameters are shown in Table I, and the inverter and grid parameters are given in Table II. In this section, the four strategies of RPCS, HMS, THCS, and the proposed HCS are tested under the same conditions.

The simulation starts with the initial conditions that the solar irradiations of five PV panels are set as: S_1=S_2=S_3=1000W/m^2, S_4=900W/m^2, S_5=750W/m^2, and the temperature is set as 25°C for each PV panel. The PV module in MATLAB/Simulink can generate P-V curves according to different irradiation levels automatically, so that the maximum output powers of five PV modules are: P_1=P_2=P_3=160W, P_4=144W, P_5=120W. Setting at 0.6s, the irradiation levels of PV module 3, PV module 4 and PV module 5 decrease to 480W/m^2, 450W/m^2, and 400W/m^2. The corresponding powers are P_1=P_2=160W, P_3=77W, P_4=72W, P_5=64W, and shown in Fig.8(a). Due to the higher input power, the $\hat{M}_i$ of the first and second HBs are increase to about 1.2, which is demonstrated in Fig.8(b). Fig.8(c) shows the grid current (i_{grid}) and grid voltage (v_{grid}) without additional control strategy. Before t=0.6s, the system operates with unity power factor, and the performance of i_{grid} is excellent. After t=0.6s, the waveform quality of i_{grid} is distorted, and the THD is 28.27%.

TABLE I
SOLAR MODULE PARAMETERS

Symbol	Parameter	Value
P_{max}	Maximum power	160W
V_{oc}	Open-circuit voltage	41.3V
I_{sc}	Short-circuit voltage	5.14A
V_{MPP}	Voltage at MPP	33.0V
I_{MPP}	Current at MPP	4.85A

TABLE II
GRID AND INVERTER PARAMETERS

Symbol	Parameter	Value
N	Number of H-bridges	5
C_i	DC bus capacitance	13.6mF
L	Filter inductance	2mH
V_m	Grid voltage peak value	130V
f_{grid}	Grid voltage frequency	50Hz
f_{car}	Switching frequency	2.5kHz

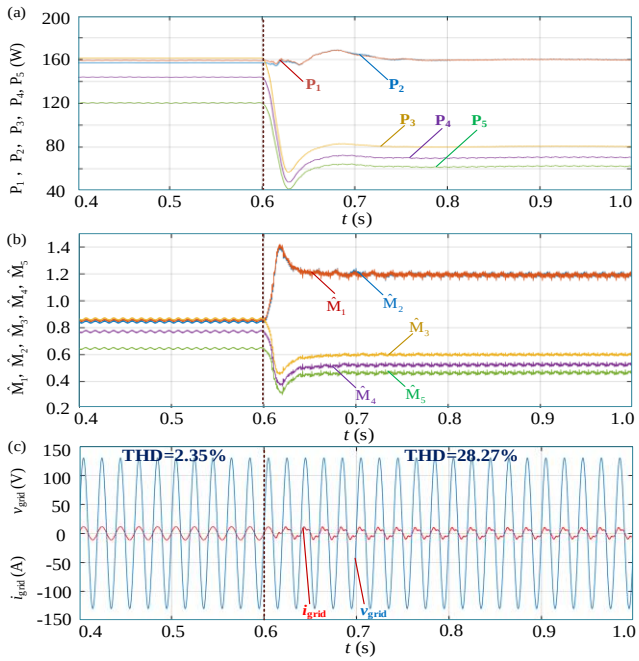

Fig.8. Simulation waveforms without additional control strategy. (a)Outpowers. (b) $\hat{M}_i$. (c)Grid current and voltage.

The next simulation with RPCS is carried out under the same conditions. The dc-link voltage and its reference of the first HB are shown in Fig.9(a), it can be seen that the voltage fluctuation does not increase after t=0.6s (The dc-link voltage before and

after t=0.6s is 0.6V). The grid current and voltage are presented in Fig.9(b), after t=0.6s, the inverter can still inject low distorted current into the grid (THD=4.36%), but it cannot operate in unity power factor.

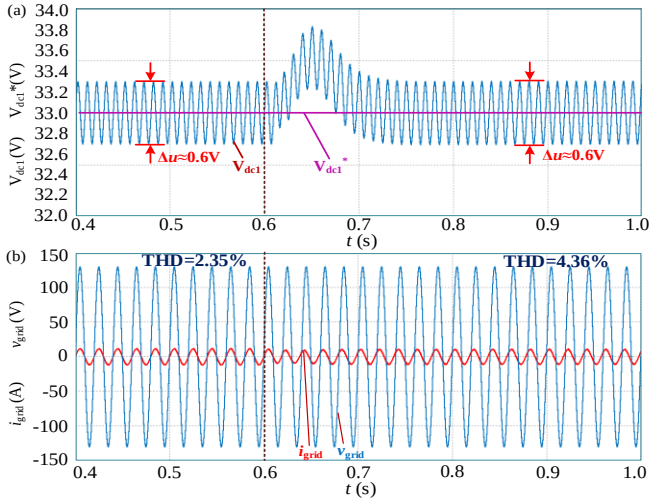

Fig.9 Simulation waveforms of RPCS. (a) dc-link voltage and its reference of the first HB. (b) Grid current and voltage.

Fig.10 reveals the simulation waveforms of HMS. After t=0.6s, the inverter can still operate in unity power factor, and the THD of grid current is only 3.35%. However, the dc-link voltage of the first HB fluctuates irregularly and sharply with the peak-to-peak value is 1.4V, which is the main drawback of HMS.

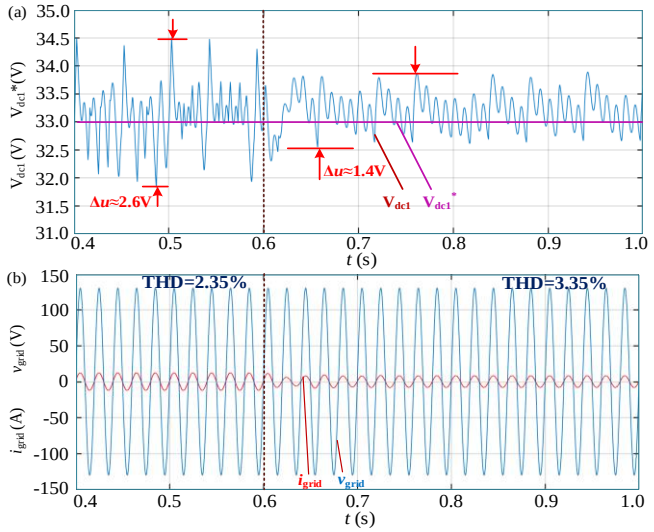

Fig.10 Simulation waveforms of HMS. (a) dc-link voltage and its reference of the first HB. (b) Grid current and voltage.

The simulation results of THCS are presented in Fig.11. Because the $\hat{M}_i$ of the first and second HBs exceed 1.155 (the maximum linear modulation range of THCS), the modulation waveform amplitudes of the first two HBs after injecting third harmonic are still larger than one, which is demonstrated in Fig.11(a). From Fig.11(b), the peak-to-peak value of the dc-link voltage is 0.6V before t=0.6s, and it does not increase after t=0.6s. Fig.11(c) is the grid current and voltage, and it can be seen that the system is operating in unity power factor before and after the power decline. The detailed waveform of i_{grid} is shown in Fig.11(d), because the modulation waveforms of the first two HBs are still overmodulation, the THD of the grid current is still high (THD=8.54%).

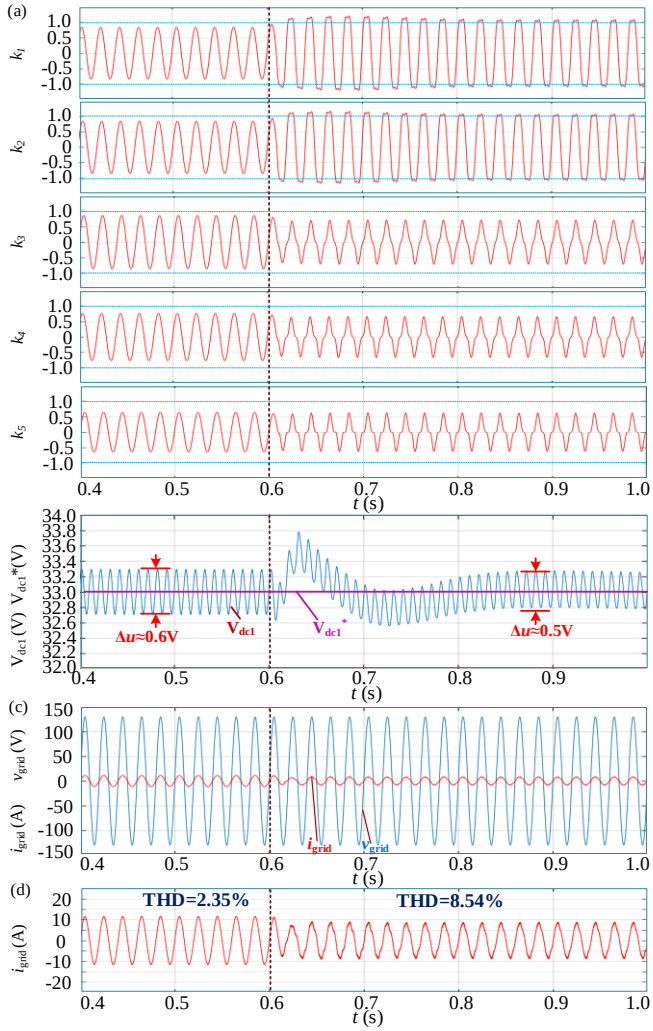

Fig.11 Simulation waveforms of THCS. (a) Modulation waveforms. (b) dc-link voltage and its reference of the first HB. (c) Grid current and voltage. (d) Grid current.

Finally, the simulation results of the proposed HCS are presented. As shown in Fig.12(a), after harmonic compensation, the modulation waveforms of the first two HBs have become quasi-square waveforms, and there is no overmodulation problem. For the last three HBs, the modulation waveforms also change because of injecting opposite harmonics. The simulation waveforms of HB_1 output voltage (v_{H1}) is shown in Fig.13(a), after t=0.6s, the output voltage of HB_1 also becomes a quasi-square waveform due to the proposed HCS. Fig.13(b) reveals the output voltage of HB_3 (v_{H3}), and its partial enlarged figure is shown in Fig.13(c). Because of injecting opposite harmonics, the modulation waveform of HB_3 has positive and negative mutations at some time, which results in the positive and negative changes of v_{H3} at some time.

Fig.12(b) reveals the dc-link voltage of the first cell, the dc-link voltage fluctuates regularly, and its peak-to-peak value is changed from 0.6V to 0.5V after t= 0.6s. From Fig.12(c) and Fig12(d), the system operates at unity power factor before and after t=0.6s, and the quality of grid current waveform remains good. The THD of i_{grid} is 2.35% before t=0.6s, and after t=0.6s,

the THD of i_{grid} has increased, but still meets the grid-connected requirements (THD=3.28%).

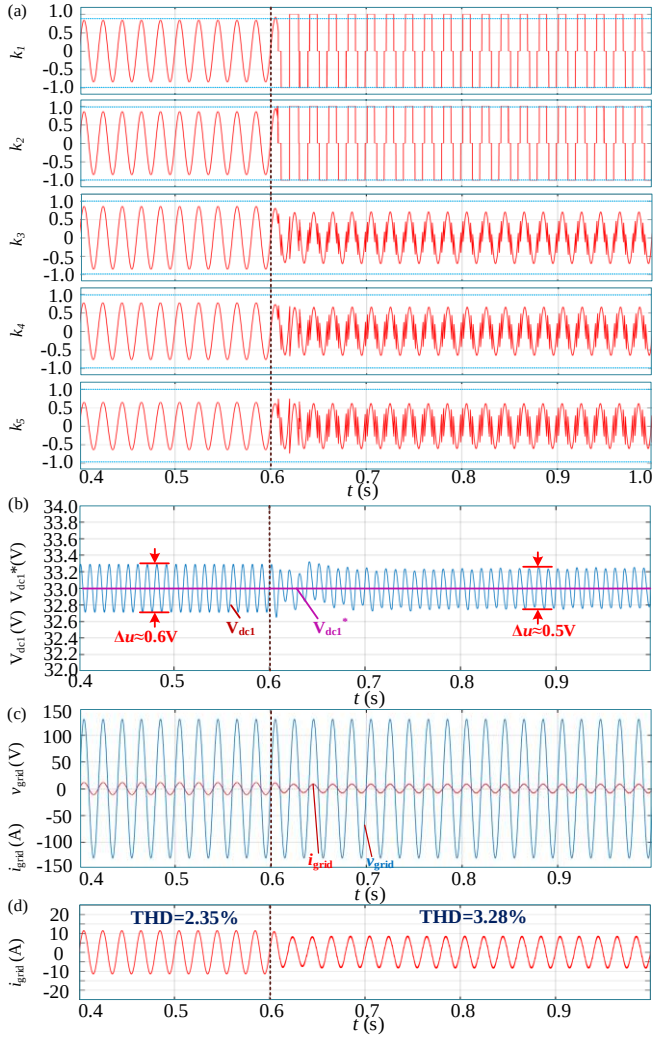

Fig.12.Simulation waveforms with HCS. (a) Modulation waveforms. (b) dc-link voltage and its reference of the first HB. (c) Grid current and voltage. (d) Grid current.

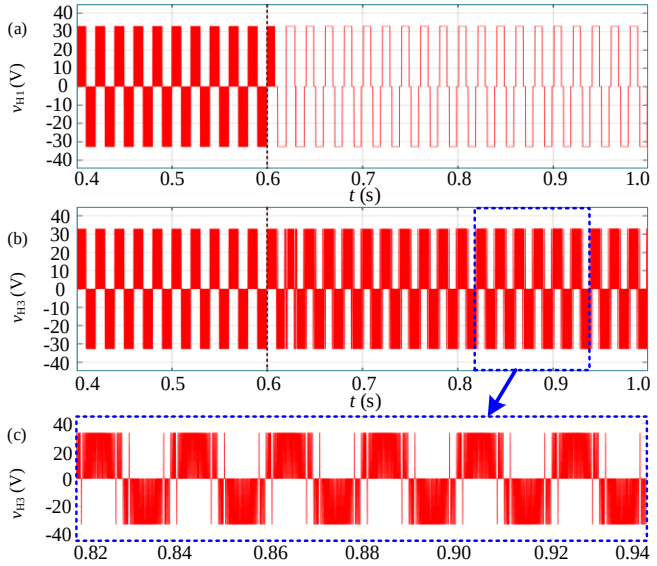

Fig.13 Simulation waveforms of v_{H1} and v_{H3} with HCS. (a) Simulation waveforms of v_{H1}. (b) Simulation waveforms of v_{H3}. (c) The partial enlarged figure of v_{H3}.

V. Experimental Results

The experimental platform of single-phase CHB PV inverter is shown in Fig.14, which is composed of five HBs. Each HB has a TMS320F28335 as an independent controller, the master controller is a BECKHOFF Industrial PC (CX2040), and every controller communicates using EtherCAT real-time communication. The control information of the platform can be observed and modified in real-time through the upper computer. The dc side of the platform uses five PV simulators Chroma62020H-150S to power the HBs, and the ac side adjusts the voltage amplitude of the power grid to 130V through the voltage regulator. Furthermore, the deadtime of each HB is set to 1.5us, and the remaining parameters are consistent with the simulation, which are given in Table I and Table II.

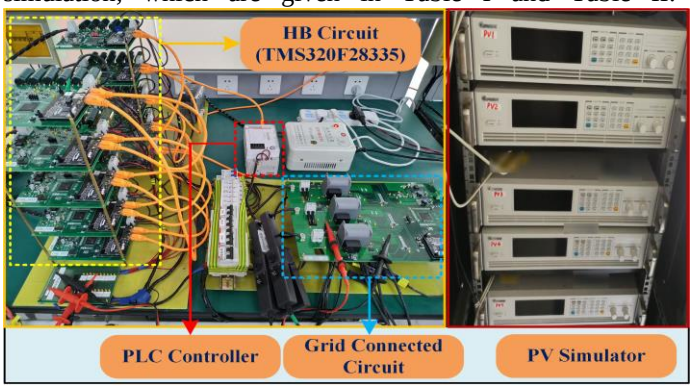

Fig.14 Experimental platform of single-phase CHB PV inverter.

The conditions for all experiments in this section are the same. At the beginning, the irradiation levels of five PV simulators are set as: S_1=S_2=S_3=1000W/m^2, S_4=900W/m^2, S_5=750W/m^2 and the environment temperatures are all 25℃. Therefore, the input powers of five HBs are: P_1=P_2=P_3≈160W, P_4≈144W, P_5≈120W. Then at some point, S_3, S_4 and S_5 are changed to 480W/m^2, 450W/m^2 and 400W/m^2, so the powers of the first two HBs are keep P_1=P_2≈160W and the third, fourth and fifth HBs are changed to P3≈77W, P4≈72W, P5≈64W. On the basis of Fig.2 and expression (9), the first and second HBs will be overmodulated.

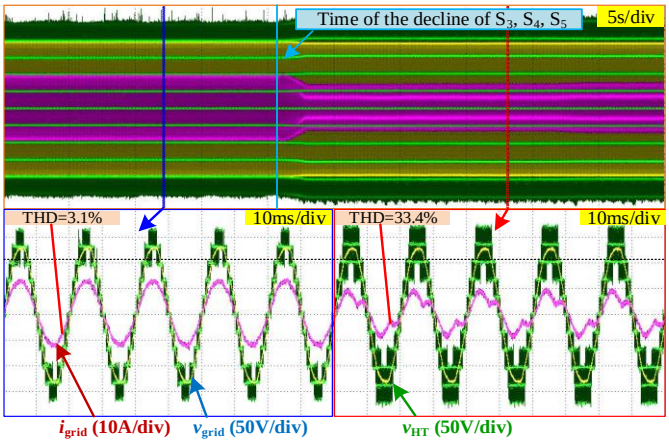

Fig.15 Experiment results of grid current (i_{grid}), grid voltage (v_{grid}) and inverter output voltage (v_{HT}) with no additional control method.

In the first experiment, no additional control method is used when the power of the system is unbalanced. The output waveform of grid current (i_{grid}), grid voltage (v_{grid}), and inverter

output voltage (v_{HT}) are presented in Fig.15. In the beginning, i_{grid} is sinusoidal and in-phase with v_{grid}, the THD of i_{grid}, which can be measured by a FLUKE 434 power quality and energy analyzer, is 3.1%. After the decline of S_3, S_4, and S_5, the highly distorted current (THD=33.4%) will be injected into grid.

Fig.16 shows the experiment results of RPCS. After the intensity of irradiance decreases, the fluctuation of the dc-link voltage is about 1V, and the THD of i_{grid} is 5.2%. However, the power factor of the system is not one.

If the HMS used, the experiment waveforms after the decline of the irradiance level are illustrated in Fig.17. The THD of i_{grid} is only 4.8%, and the system can operate at unity power factor. But the dc-link voltage fluctuates irregularly and sharply with the peak-to-peak value is 1.5V.

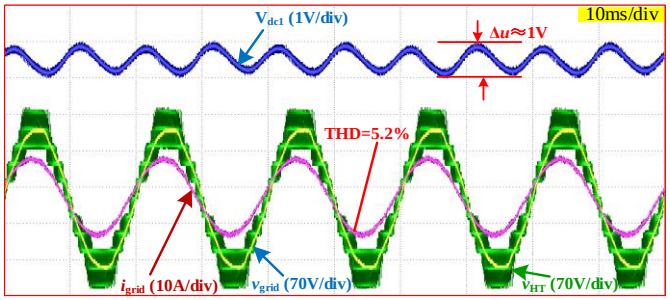

Fig.16 Experiment waveforms of RPCS.

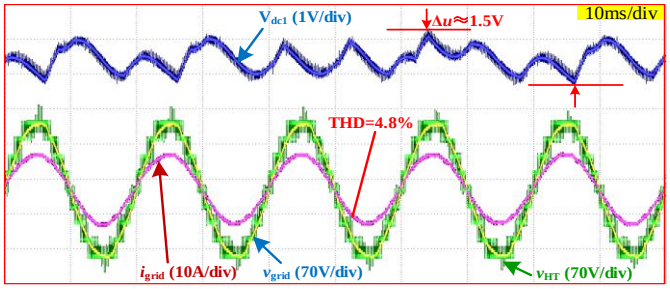

Fig.17 Experiment waveforms of HMS.

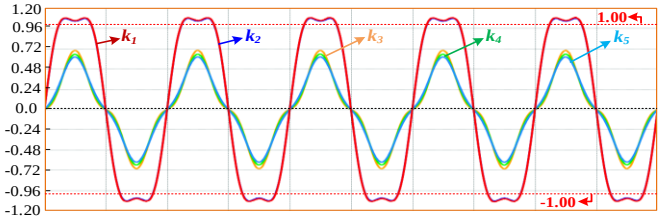

Fig.18 Experiment results of modulation waveforms of THCS.

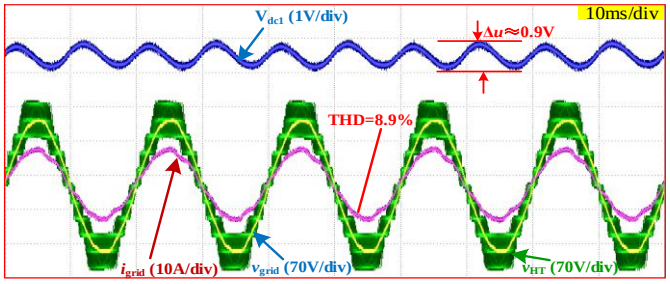

Fig.19 Experiment results of grid current (i_{grid}), grid voltage (v_{grid}) and inverter output voltage (v_{HT}) using THCS.

For THCS, its experimental waveforms are presented in Fig.18 and Fig.19. After the decrease of S_3, S_4 and S_5, because this power unbalance condition has exceeded the linear modulation range of THCS, the modulation waveform amplitudes of the first two HBs are still greater than one (as shown in Fig.18), which result in the CHB inverter with THCS inject a highly distorted current into the grid (THD=8.9% in steady-state). The fluctuation of dc-link voltage is 0.9V after the power decline (as shown in Fig.19).

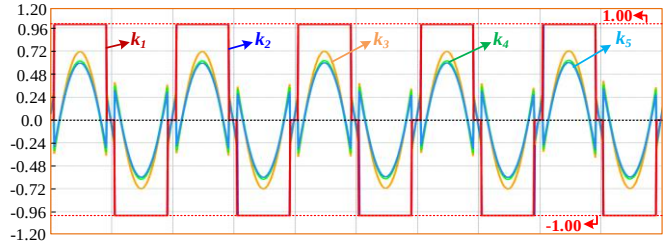

Fig.20 Experiment results of modulation waveforms of HCS.

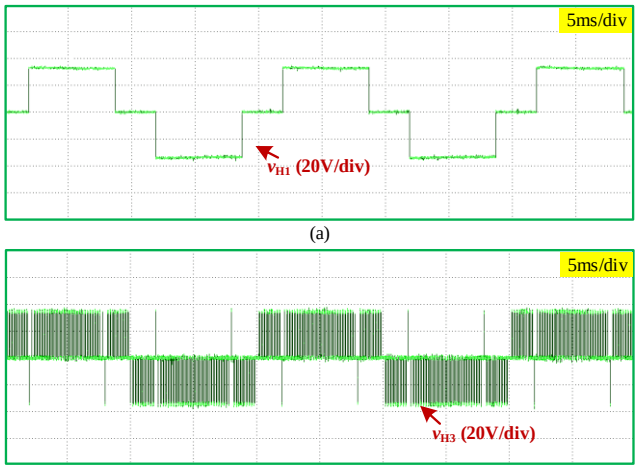

Fig.21 Experiment waveforms of v_{H1} and v_{H3} with HCS. (a) Experiment waveforms of v_{H1}. (b) Experiment waveforms of v_{H3}.

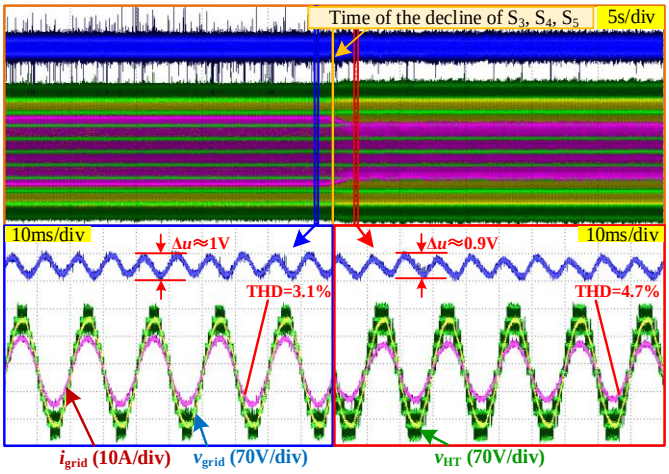

Fig.22 Experiment waveforms of HCS.

In the final experiment, the proposed HCS is used when the power of the system is unbalanced. Fig.20 illustrates the modulation waveforms of each HB after the decline of the irradiance level. It is observed that harmonics compensates the modulation waveforms of HB_1 and HB_2 into quasi-square waveforms with the amplitude of one, and the modulation waveforms of HB_3, HB_4 and, HB_5 are superimposed with inverse harmonics. The output voltages of HB_1 and HB_3 when HCS is adopted are shown in Fig.21. Fig.21(a) is the experiment waveforms of v_{H1}, which corresponds to the

simulation results in the Fig.13(a), and Fig.21(b) reveals the experimental results of v_{H3}. It can be seen that v_{H3} also has positive and negative mutations. In Fig.22, the remaining experiment waveforms of HCS is presented. The sub-figure in the lower-left corner shows the detailed waveforms before power decline, and the detailed waveforms after power decline are shown in the lower-right sub-figure. As could be seen, after the decline of S_3, S_4, and S_5, the system still operates at unity power factor, and the quality of i_{grid} remains good (THD=4.7%). The dc-link voltage fluctuates regularly, and its peak-to-peak value is changed from 1V to 0.9V.

The detailed dynamic transition of HCS is shown in Fig.23 and Fig.24. Fig.23 is the dynamic transition of i_{grid} from normal modulation region to the over-modulation region, and the opposite process is presented in Fig.24. From these two experiment results, the transition process is relatively gentle.

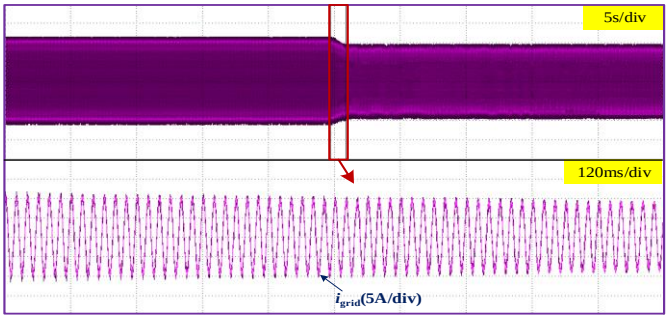

Fig.23 Experiment waveforms of dynamic transition with HCS (From normal modulation region to the over-modulation region).

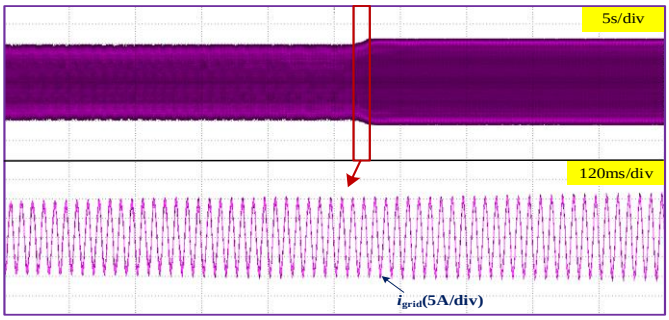

Fig.24 Experiment waveforms of dynamic transition with HCS (From over-modulation region to the normal modulation region).

VI. CONCLUSION

In this paper, a harmonic compensation strategy that allows single-phase CHB PV inverters to operate generally under power imbalance is proposed. This strategy ensures that the CHB inverter can operate at unity power factor and extend its linear modulation range to about 1.27. In some cases of severe power imbalance, the strategy still maintains the grid current to meet the requirements. Both simulation and experiment verify the effectiveness of the proposed strategy.

Reference

[1] X. Zhang, T. Zhao, W. Mao, D. Tan, and L. Chang, "Multilevel inverter for grid-connected photovoltaic applications: examining emerging trends," *IEEE Power Electronics Magazine*, vol. 5, no. 4, pp. 32-41, Dec. 2018.

[2] J. Ebrahimi, E. Babaei, and G. B. Gharehpetian, "A new topology of cascaded multilevel converters with reduced number of components for high-voltage applications," *IEEE Trans. Power Electron.*, vol. 26, no. 11, pp. 3109–3118, Nov. 2011.

[3] J. Rodriguez, S. Bernet, W. Bin, J.O. Pontt, and S. Kouro, "Multilevel voltage-source-converter topologies for industrial medium-voltage drives," *IEEE Trans. Ind. Electron.*, vol. 54, no. 6, pp. 2930-2945, Dec. 2007.

[4] P. Hongbin, Z. Hongzhang, X. Zhiyong, "A novel DC voltage and reactive power balance control strategy for cascaded H bridge rectifier," *Proceedings of the CSEE.*, vol. 37, no. 12, pp. 3565–3573, 2017.

[5] C. Cecati, F. Ciancetta, and P. Siano. "A multilevel inverter for photovoltaic systems with fuzzy logic control," *IEEE Transactions on Industrial Electronics*, vol. 57, no. 12, pp. 4115–4125, Dec, 2010.

[6] X. Bailu, H. Lijun, and M. Jun, "Modular cascaded H-bridge multilevel PV inverter with distributed MPPT for grid-connected applications," *IEEE Transactions on Industry Applications.*, vol. 51, no. 2, pp. 1722-1731, 2015.

[7] E. Babaei, S. Laali, and S. Alilu, "Cascaded multilevel inverter with series connection of novel H-bridge basic units," *IEEE Transactions on Industrial Electronics*, vol. 61, no. 12, pp. 6664-6671, Dec. 2014.

[8] Y. Yu, G. Konstantinou and B. Hredzak, "Power balance of cascaded H-bridge multilevel converters for large-scale photovoltaic integration," *IEEE Transactions on Power Electronics*，vol. 31, no. 1, pp. 292-303, Jan. 2016.

[9] O. Alonso, P. Sanchis, E. GubíaL, and L. Marroyo, "Cascaded H-bridge multilevel converter for grid-connected photovoltaic generators with independent maximum power point tracking of each solar array," *IEEE Power Electronics Specialist Conference.* 2003.

[10] L. Liu, H. Li, and Y. Xue, "A coordinated active and reactive power control strategy for grid-connected cascaded photovoltaic (PV) system in high voltage high power applications," in Proc. IEEE 28th Appl. Power Electron. Conf. Expo., Long Beach, CA, USA, Mar. 17–21, 2013, pp. 1301–1308

[11] M.A Rezaei, S. Farhangi, and H. Iman-Eini, "Extending the operating range of cascaded H-bridge based multilevel rectifier under unbalanced load conditions," *IEEE International Conference on Power & Energy*, Nov.2010, pp.780-785.

[12] A. Eskandari, V. Javadian, and H. Iman-Eini, "Stable operation of grid connected Cascaded H-Bridge inverter under unbalanced insolation conditions," *International Conference on Electric Power & Energy Conversion Systems. IEEE*, 2014.

[13] M. Moosavi, G. Farivar, H. Iman-Eini, "A voltage balancing strategy with extended operating region for cascaded H-bridge converters," *IEEE Transactions on Power Electronics*, vol. 29, no. 9, pp. 5044-5053, Sep. 2014.

[14] M. Miranbeigi, H. Iman-Eini, "Hybrid Modulation Technique for Grid-Connected Cascaded Photovoltaic Systems," *IEEE Transactions on Industrial Electronics*, vol. 63, no. 12, pp. 7843-7853, Dec. 2016.

[15] T. Zhao, X. Zhang, W. Mao, F. Wang, J. Xu, and Y. Gu, "A modified hybrid modulation strategy for suppressing dc voltage fluctuation of cascaded H-bridge photovoltaic inverter," *IEEE Trans. Ind. Electron.*, vol. 65, no. 5, pp. 3932-3941, May. 2018.

[16] W. Mao, X. Zhang; Y. Hu, T. Zhao, F. Wang, F. Li, and R. Cao, "A Research on Cascaded H-Bridge Module Level Photovoltaic Inverter Based on a Switching Modulation Strategy", Energies 2019, 12, 1851.

[17] W. Fusheng, Z. Dehui, D. Zhiqiang, "A hybrid control scheme of cascaded H-bridge inverter for grid-connection photovoltaic systems," *Transactions of China Electrotechnical Society*, vol. 31, no.1, pp. 137-145, 2016.

[18] L. Liu, H. Li, and Y. Xue, "Reactive Power Compensation and Optimization Strategy for Grid-Interactive Cascaded Photovoltaic Systems," *IEEE Transactions on Power Electronics*, vol. 30, no.1, pp. 188-202, Jan.2015.

[19] L. Liu, H. Li, and Y. Xue, "Decoupled Active and Reactive Power Control for Large-Scale Grid-Connected Photovoltaic Systems Using Cascaded Modular Multilevel Converters," *IEEE Transactions on Power Electronics*, vol. 30, no.1, pp. 176-187, Jan.2015.

[20] T. Zhao, X. Zhang, W. Mao, et al, "Control Strategy for Cascaded H-Bridge Photovoltaic Inverter Under Unbalanced Power Conditions Based on Reactive Compensation," *Proceedings of the CSEE*, vol. 37, no.17, pp. 5076-5085, 2017.

[21] Yu. Y, G. Konstantinou, B. Hredzak, et al, "On extending the energy balancing limit of multilevel cascaded H-bridge converters for large-scale

photovoltaic farms," *Australasian Universities Power Engineering Conference (AUPEC)*, 2013.
[22] B. Xiao, L. Hang, J. Mei, et al. "Modular Cascaded H-Bridge Multilevel PV Inverter with Distributed MPPT for Grid-Connected Applications", IEEE Transactions on Industry Applications, vol. 51, no. 2, pp. 1722-1731, Mar/Apr.2015
[23] Y. Hu, X. Zhang, W. Mao, T. Zhao, et al, "An Optimized Third Harmonic Injection Method for Reducing DC-link Voltage Fluctuation and Alleviating Power Imbalance of Three-Phase Cascaded H-Bridge Photovoltaic Inverter," *IEEE Transactions on Industrial Electronics*, early access, 2019.
[24] Y. Ko, M. Andresen, and G. Buticchi, "Power Routing for Cascaded H-Bridge Converters," *IEEE Transactions on Power Electronics*, vol. 32, no.12, pp. 9435-9446, Dec.2017.
[25] T. Zhao, X. Zhang, W. Mao, F. Wang, et al., "An Optimized Third Harmonic Compensation Strategy for Single-Phase Cascaded H-Bridge Photovoltaic Inverter," *IEEE Transactions on Industrial Electronics*, vol. 65, no. 11, pp. 8635-8645, Nov. 2018.

Mingda Wang was born in Anhui, China, in 1996. He received the B.S degree in electrical engineering and automation from Hefei University of Technology, Hefei, China, in 2017. And he is currently working toward the Ph.D. degree in electric engineering from the School of Electrical Engineering and Automation, Hefei University of Technology, Hefei, China.

His current research interests include the control of power converters, and photovoltaic generation technologies.

Xing Zhang (M'13-SM'14) was born in Shanghai, China, in 1963. He received the B.S., M.S. and Ph.D. degrees in electric engineering and automation from Hefei University of Technology, Hefei, China, in1984, 1990, and 2003, respectively.

Since 1984, he has been a Faculty Member of the School of Electric Engineering and Automation, Hefei University of Technology, where he is currently a Professor and also serves as the Chief of National and Local Joint Engineering Laboratory for Renewable Energy Access to Grid Technology. He is also with the Photovoltaic Engineering Research Center of Ministry of Education.

His main research interests include photovoltaic generation technologies, wind power generation technologies, and distributed generation system.

Tao Zhao (S'17) was born in Henan, China, in 1991. He received the B.S. degree in electrical engineering and Automation from Xi'an Technological University, Xi'an, China and the M.S. degree in power electronics and power drives from Hefei University of Technology, Hefei, China, in 2014 and 2017, respectively. He is currently working toward the Ph.D. degree in electrical engineering in Hefei University of Technology.

His current research interests include the modeling and control of power converters, and multilevel converters

Mingyao Ma (M'11) received the B.Sc. and Ph.D. degrees in applied power electronics and electrical engineering from Zhejiang University, Hangzhou, China, in 2004 and 2010, respectively. From October 2008 to October 2009, she was a visiting PhD postgraduate research student in the University of Strathclyde, Glasgow, U.K., and in 2010, she joined Zhejiang University as a Post-Doctoral Research Fellow. In 2011, she worked for the University of Central Florida, Orlando, US, as the visiting scholar. From April 2012 to April 2015, she joined the Newcastle University, Newcastle, UK, as the Research Associate. From 2015 she works in Hefei University of Technology as a professor. Her research interests include multilevel converters, distributed control of PEBB-based converters, software design using FPGA and DSP, SR motor control, and health monitoring and fault diagnostic technique of power electronics systems.

Yuhua Hu was born in Anhui, China, in 1994. He received the B.S. degree in electrical engineering from the School of Electrical Engineering and Automation, Anhui University, Hefei, China, in 2017. He is currently working toward the M.S. degree in electric engineering and automation in Hefei University of Technology.

His current research interests include the modeling and control of power converters, and photovoltaic generation technologies.

Fusheng Wang (M'13) was born in Anhui, China, in 1976. He received the B.S. degree in electric engineering and automation from Hefei University of Technology, Hefei, China, in 1998, and the Ph.D. degree in nuclear science and engineering from Institute of Plasma Physics Chinese Academy of Sciences, Hefei, in 2005. In 2006, he joined the Faculty of the School of Electric Engineering and Automation, Hefei University of Technology, where he is currently an Associate Professor.

His current research interests include control of multilevel converters, and photovoltaic generation technologies.

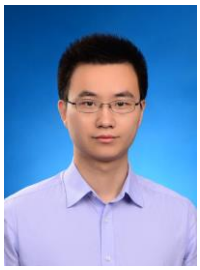

Xinyu Wang received the B.S. degree in electric and information engineering from Zhejiang University, Hangzhou, China, in 2009, and the Ph.D. degree in electrical engineering from Xi'an Jiaotong University, Xi'an, China, in 2015. From 2015 to 2016, he was a Lead Engineer with Corporate Research and Technology, Eaton, Shanghai, China. He is currently a Senior Engineer with the Corporate Research Institute, Sungrow Power Supply Company, Ltd., Hefei, China.

His main research interests include multilevel converter, power electronic transformer, and power electronics applications in renewable energy and distributed generation.